Design of the All-Electric Ship: Focus on Integrated Power System coupled to Hydrodynamics

P. Prempraneerach[1,4], J. Kirtley[2], C. Chryssostomidis[1], M.S. Triantafyllou[3] and G.E. Karniadakis[3,5]
[1]MIT Sea Grant College Program
[2]Department of Electrical Engineering and Computer Science
[3]Department of Mechanical Engineering
Massachusetts Institute of Technology, Cambridge, MA, USA 02138
[4]Department of Mechanical Engineering
Rajamangala University of Technology Thunyaburi, Pathumthani, Thailand 12110
[5]Division of Applied Mathematics
Brown University, Providence, RI, USA 02912

ABSTRACT

We present a detailed model of the integrated power system coupled to hydrodynamics that allows us to study global sensitivities in the All-Electric Ship. A novel element of our formulation is the stochastic modeling of the coupled system to account for uncertainty in the parameters or operating conditions. This new computational framework is applied to a model of the DDG-51 destroyer that involves a 19 MW 15-phase induction machine and an indirect field oriented controller. In particular, we simulate extreme events corresponding to propeller emergence and firing of pulsed power weapons.

1. INTRODUCTION

In the All-Electric Ship (AES) architecture, the power sharing between the propulsion units and the high-power equipment, especially under heavy propulsion demands and casualty conditions, has recently been identified as an important design issue [6], [27], [35]. In the new AES configuration, there is an increasing demand for electric power for ship system automation, electrical weaponry, electric propulsion, and ship service distribution. About 70% to 90% of power from the generator units in the fully integrated power system (IPS) is consumed in the propulsion systems [6]. Therefore, when a large power demand is imposed on an electrical bus during a mission or life critical situation, the power distribution must be optimally modified to yield the most efficient power usage and to maintain continuity of service [35].

This complex problem is compounded by the sea states which are unpredictable, leading to stochastic time-varying propulsion loads. It is, therefore, challenging for the electric ship designer to thoroughly investigate interactions between machines, power electronics, and uncertain sea conditions. To date there have been no published papers that account for *dynamic* interactions of propeller and ship hydrodynamics with a large-scale shipboard IPS. In this paper, we develop stochastic models of the IPS and the propeller coupled to random wave dynamics and ship motion. In the following, we present some details of the system that we model, the technical approach, and first results.

2. SYSTEM MODELING

To investigate the influence of the propeller loading and the pulsed power load on the AC propulsion and power generation in the electric ship, modeling of both power systems and hydrodynamics of ship and propeller must be introduced. In our study, the IPS is similar to the model described in [29] for a destroyer class. In summary, the main AC subsystem of this IPS consists of a 21 MW, 3-phase, 60Hz Synchronous Machine (SM) as a generator, a close-loop drive using the indirect rotor field oriented control of 19 MW, 15-phase Induction Machine (IM) as a propulsor, and a pulsed power charger for an EM gun. The generator supplies the voltage to the 3-phase 4160V AC distribution bus, which must be filtered by a harmonic filter before connecting to the induction motor drive. The detailed derivation of machine equations can be found in [22] and [29]. A power converter and the Indirect Field Oriented Control (IFOC) using the sine-triangle modulation technique for

a current regulator are incorporated into the propulsion system to control the torque of the induction machine. According to [14], the IFOC employs an inner loop with a current feedback from IM and an outer loop with IM's shaft angular velocity feedback for computing the machine rotational angle in the IFOC. The IPS configuration considered in this study is similar to a split plant arrangement in [4], shown in Figure 1. In the split plant configuration, a single high-power generator supplies power to a propulsion unit, one EM gun and a gun support service. On the other hand, two high-power generators connect through AC distribution bus to support two propulsions and two EM gun in the parallel plant arrangement. Also, a schematic of the IPS installed in the ship we model here is shown in Figure 2.

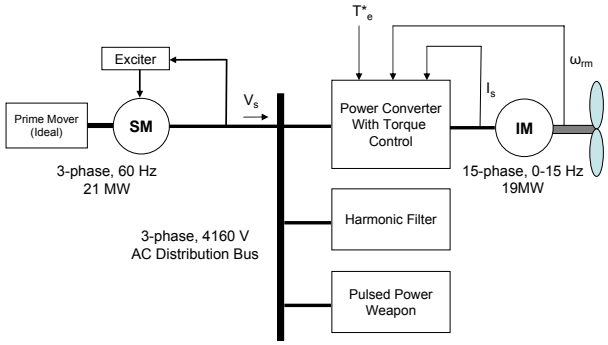

Figure 1. A one-line diagram of the AC power generator and power distribution with the closed-loop torque control of the induction machine.

2.1. Hydrodynamics

The propeller model, used in this study, is based on a five-blade, fixed-pitch, highly skewed propeller with a maximum skew angle of 32 degrees [1]. Several effects, such as fluctuation of in-line water inflow, ventilation, and in-and-out-of water effects [21], can cause a reduction in the propeller thrust and torque from its nominal operating condition. Both the in-line water inflow variation and the in-and-out-of water effects directly affect the propeller loading. The propeller emergence can abruptly reduce the propeller thrust because of a loss in the propeller effective disc area. Especially, when the ship operates in the rough sea condition, the propeller emergence can occur intermittently, resulting in ship speed reduction, sudden increase in shaft angular

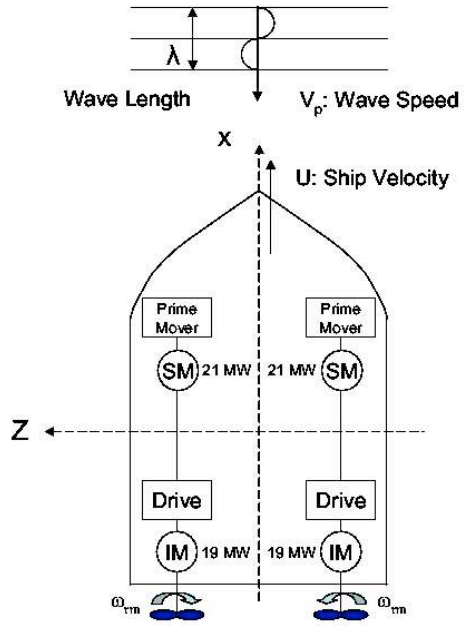

Figure 2. A diagram of the ship motion in the surge direction within the head sea.

speed, and rapid decrease in motors' current. Propeller thrust and torque loss can be represented by the thrust loss factor, β_T, and the torque loss factor, β_Q, multiplied by the open-water propeller thrust, T_p, and torque, Q_p, respectively. According to [21], the thrust loss factor due to the propeller emergence is assumed to be proportional to the effective disc area as follows:

$$\beta_T = real\Big(1 - \frac{\arccos(\frac{h}{R})}{\pi} + \frac{\frac{h}{R}}{\pi}\sqrt{1-(\frac{h}{R})^2}\Big), \qquad (1)$$

where h/R is the relative submergence, with h the propeller shaft submergence and R the propeller radius. Thus, we have $\beta_T = 1$ when the propeller is fully submerged. Also, β_Q, corresponding to a reduction of the effective propeller disc area, and it is related to β_T as follows:

$$\beta_Q = (\beta_T)^m,\ 0 < m < 1, \qquad (2)$$

where for an open-water propeller, m is typically within the range of 0.8 and 0.85, resulting in a larger β_Q than β_T, such that the propeller efficiency is less than unity if the loss due to propeller emergence increases.

To model the *wave effects*, first, we assume that nonlinear and viscous effects are small compared to

Table 1. Specifications of the DDG 51 Flight I.

Parameters	full-scale DDG-51
Length [m]	153.90
Draft [m]	9.45
Beam [m]	20.12
Displacement [tons]	8,300
Speed [knot]	31
Propeller Diameter [m]	5.20
Propulsion Power [hp]	100,000

wave inertia for a ship motion in the sea. Moreover, we assume that deep water random waves, modeled through the one-parameter Pierson and Moskowitz spectrum [13], derived on the basis of North Atlantic data and described by the significant wave height, $H^{1/3}$.

To model *ship hydrodynamics*, we must consider the interaction between the propeller and ship hull because the wake created by the hull modifies the propeller advance velocity (V_a) [17] with $V_a = (1-w)U$, where U is the ship speed. The wake fraction ($0 < w < 0.4$) [17] indicates the velocity reduction due to the wake; here we used $w = 0.2$. Moreover, the presence of the propeller at the stern also increases the drag force on the vessel; thus, the propeller thrust must be decreased by a factor $(1-t_d)$, where t_d is the so-called "thrust deduction factor" to account for the difference between the self-propelled and the towed-model resistance; in this study we used $t_d = 0.2$.

The specifications of the full-scale USS DDG-51 Arleigh Burke-class [15], driven by the electrical propulsor, are given in Table 1. This full-scale ship is employed in the ship hydrodynamics calculations for calm water and added resistances, and for propeller performance.

In this study, we consider only the *surge motion* of the electric ship, driven by two propellers connected to two identical IPS, in head sea. We note that the total propulsion system of DDG-51 consists of 4 identical IPS and achieves 31 knots; with two IPS it achieves a maximum speed of about 24 knots. The ship's motions in other directions i.e., sway, heave, roll, pitch, and yaw are assumed to be small. Thus, the equation of ship motion with the induction motor directly driven the propeller can be described as:

$$\begin{aligned}(M+M_a)\frac{dU(t)}{dt} &= 2(1-t_d)T_p(n,U) - R(U) \\ &\quad -\bar{R}_{AR}(U) - R_{2nd-AR}(U,t), \end{aligned} \tag{3}$$

$$J_s\frac{d\omega_r(t)}{dt} = T_e - Q_p(n,U)\eta_b\eta_r, \tag{4}$$

where n denotes revolutions per minute of the propeller, $n = \omega * 30/\pi$, and M and M_a are the ship mass and added mass in the surge direction, respectively. The rotational inertia, J_s, includes the IM rotor and propeller inertia; also, T_p and Q_p are the propeller open-water thrust and torque, respectively, i.e., $T_p = K_T(J)\rho n^2 D^4$ and $Q_p = K_Q(J)\rho n^2 D^5$, where $J = \frac{V_a}{nD}$ is the advance velocity. Also, K_T and K_Q are thrust and torque coefficients of the propeller, while η_b and η_r denote the bearing and propulsive efficiency. The drag force, R, corresponds to the calm-water resistance; it can be found from the non-dimensional drag coefficient, $C_D(Re,Fr)$, as $R = C_D\frac{1}{2}\rho S U^2$ where S is the wetted surface area. The drag coefficient C_D [13] is composed of a frictional resistance coefficient ($C_F(Re)$) and a residual resistance coefficient ($C_R(Fr)$), where Re and Fr are Reynolds and Froude numbers, respectively. The added resistance, R_{AR}, is associated with the involuntary speed reduction due to the waves. Assuming that the added resistance is a second-order nonlinear system obeying the properties of quadratic systems, the slowly-varying added resistance can be separated into two major components: *mean* or steady second-order force ($\bar{R}_{AR}$) (the first term) and *slowly-varying* second-order force (R_{2nd-AR}) (the second term), given by:

$$R_{AR} = \bar{R}_{AR} + R_{2nd-AR} \tag{5}$$

$$\begin{aligned}R_{AR} &= \frac{1}{2}\sum_{k=1}^{N}(A_k)^2 H(\omega_k,-\omega_k) + \\ &\quad \frac{1}{2}\sum_{k=1}^{N}\sum_{l=1}^{N} Re\{A_k A_l H(\omega_k,\omega_l)e^{i[\Delta\omega t+\Delta\phi]}\}\end{aligned} \tag{6}$$

where $\Delta\omega = \omega_k - \omega_l$ and $\Delta\phi = \phi_k - \phi_l$, and $\phi_{k,l}$ are wave amplitudes and independent random phases varying between $(0, 2\pi)$, respectively, corresponding to the wave frequency $\omega_{k,l}$. Note that A_k can be calculated from the one-side sea spectrum ($S^+(\omega)$) by discretizing $S^+(\omega)$ into N equally intervals. Then, $A_k^2 = 2\int_{\omega_{k+1}}^{\omega_k} S^+(\omega)d\omega$ for

$k \in 1,...,N$. $H(\omega_k, \omega_l)$ represents the second-order transfer function of hydrodynamics force. The response amplitude of the steady force normalized by the wave amplitude squared is denoted by $R(\omega)$; therefore, $R(\omega)$ is assumed to be equal to $\frac{1}{2}H(\omega_k, -\omega_k)$. According to [20], the mean added resistance is obtained from $R(\omega)$, and it is computed from the MIT5D Code [5]. For the slowly-varying added resistance, $H(\omega_k, \omega_l)$ can be approximated as $2R(\frac{\omega_k+\omega_l}{2})$. From Newman's approximation [18], R_{2nd-AR} is associated with the diagonal terms of $H(\omega_k, \omega_l)$ if the difference of the two-frequency wave, ω_k and ω_l, is very small, e.g., $|\omega_k - \omega_l| < 0.2$.

Table 2. Parameters of the 21 MW, 3-phase, 60-Hz synchronous machine [29] in SI unit system.

$r_s = 1.27m\Omega$	$L_{ls} = 369\mu H$	$L_{mq} = 2.51mH$
$L_{md} = 2.79mH$	$r_{kq} = 5.26m\Omega$	$L_{lkq} = 157\mu H$
$r_{kd} = 4.74m\Omega$	$L_{lkd} = 69.8\mu H$	$r_{fd} = 401\mu\Omega$
$L_{lfd} = 227\mu H$	$P = 2$	

2.2. Integrated Power System (IPS)

The first major component of IPS is the **synchronous generator** or machine (SM), which supplies electric power to AC power distribution and propulsion system. The mathematical model of a 3-phase, salient-pole synchronous machine consists of the rotor windings - the field winding (fd), damper windings (kq and kd) - and the symmetrical stator windings ($qs, ds, 0s$). The detailed equations are given in [22, 29] and the parameters we used are shown in table 2 .

To maintain the bus voltage at a specified level, an **exciter** is needed to feedback the bus voltage to the generator. The exciter/voltage regulator, controlling the field winding of the generator, is modeled according to a simplified model of the IEEE type 2 [12]. This type of exciter is typically accepted in the industry due to the model's simplicity. The main components of this exciter are an independent power supply, a self-excited shunt field, a stabilization feedback associated with gains and time constants, and a nonlinear saturation in the shunt field. The state equations for this type of exciter are described in [22, 29] and the parameters used are shown in table 3.

Table 3. Parameters of the IEEE Type 2 exciter [29]

$v_{ref} = 4160V$	$v_{Rmax} = 7.37p.u.$	$v_{Rmin} = 0p.u.$
$K_F = 0.03$	$K_A = 400$	$T_A = 20ms$
$K_E = 1.0$	$T_E = 0.8s$	$T_{F1} = 1.0s$
$T_{F2} = 1.0s$	$A_{Ex} = 0.14$	$B_{Ex} = 1.75$
$T_R = 1ms$		

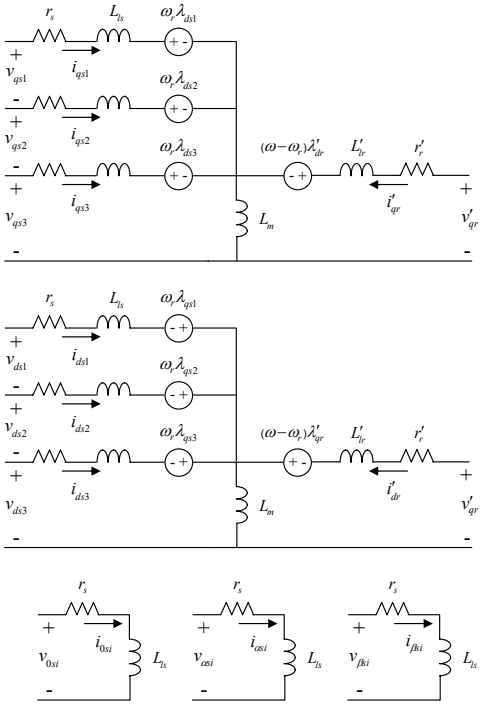

Figure 3. Three 5-phase equivalent circuits of 15-phase induction machine in the $qd0\alpha\beta$ synchronous reference frame, where $i \in 1,...,5$.

The propulsion system of IPS is driven by a 19 MW, 15-phase (squirrel cage) **induction machine**. The larger number of phases in the induction motor is, the larger the electromagnetic torque is and hence a more reliable motor operation can be achieved. In this study, the model of the 15-phase induction machine is represented by three 5-phase equivalent circuits in the $qd0\alpha\beta$ reference frame, introduced in [29], such that the quantities in the $0\alpha\beta$ axis are independent of those in qd axis. The three 5-phase equivalent circuits of the 15-phase induction machine are represented in Figure 3. This shows that the qd-axis stator and rotor voltages are highly cou-

Table 4. Parameters of the 19 MW, 15-phase induction machine [29] in SI unit system

$r_s = 122m\Omega$	$L_{ls} = 6.79mH$	$L_m = 145mH$
$r_r^{'} = 35.7m\Omega$	$L_{lr}^{'} = 7.62mH$	$P = 12$

pled and nonlinear. All parameters of the 15-phase induction machine are given in table 4.

Indirect Field Oriented Control (IFOC) of the 15-phase induction motor drive requires an input torque command (T_e^*) and a desired rotor flux command (λ_{dr}^{e*}) and outputs semiconductor signals, driving the H-bridge type inverters. Because of the multiple phases in the induction motor, the power converter topology must be separated into three five-phase parallel rectifier-dc link-inverter paths, as shown in Figure 4. As a result, each of the five phases of the induction machine can be independently controlled using the paralleling control. The dc voltage from a six-pulse uncontrolled rectifier (v_{r_j}) in each path or rail (j) must be filtered with a low-pass LC circuit before propagating to five ith H-bridges inverters. In each rail, the smoothed dc voltage (v_{dc_j}) can be expressed by $\mathbf{v}_{dc} = [v_{dc_1}, v_{dc_2}, v_{dc_3}]$ where $j = 1,2,3$. Then, the dc current (i_{dc_j}) in each rail is a summation of five ith H-bridge current (i_{dch_i}). In each rail, the phase of the ith H-bridge in Figure 4 is determined so that the AC voltage of ith H-bridge is displaced by $(i-1)24^\circ$ from the first phase. Each H-bridge is composed of four controllable semiconductor switches, denoted as D_{1_i} through D_{4_i}.

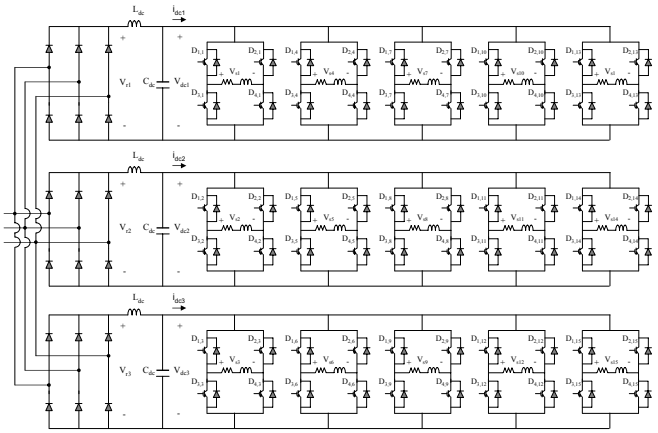

Figure 4. A diagram of the three five-phase rectifier-dc link-inverter path in the power converter.

In this study, maintaining the induction machine's *torque* at a specified level is the main objective of IFOC. According to [29], this control technique must be stable, the current be constrained below a maximum semiconductor current limit, the switching frequency be kept constant at 2 kHz, and the IFOC act as a torque transducer. Thus, the structure of the field oriented control, shown in Figure 5, consists of 6 main parts: a paralleling control, a torque limiter, a dc link stabilizing control, a current limiter, a field oriented supervisory control, and a current regulator. Five-phase inverter-rail voltages are controlled by the three independent control architectures in the IFOC. Although there might exist a negative impedance instability in the dc link due to the tight control of switch current, the IFOC's fast response can help stabilize the power converter. Details regarding the diagrams and corresponding governing equations of the paralleling control, torque limiter, and current limiter are given in [29]; the parameters used are shown in table 5.

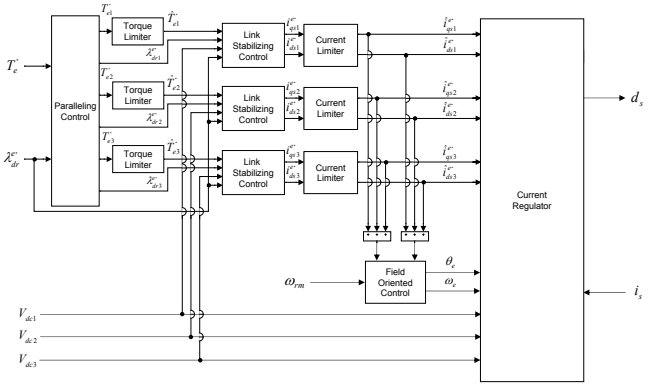

Figure 5. The link stabilized and indirect field oriented controller.

We also model the **pulsed power weapon** system and for this a 6-pulse rectifier and an LC pulse forming network and its controller must be modeled such that a specific voltage profile for charging a storage capacitor can be supplied. Figure 6 shows the charging profile of capacitor voltage; it increases linearly during the charging interval, t_{cha}, then the voltage is held constant for a capacitor to be fully charged in the catch-up period, t_{ca}. After the commutating period of thyristor, t_{off}, the capacitor is now ready to instantly discharge to the pulsed load. The model of the pulsed power charger is

Table 5. Parameters of the indirect field oriented controller for 15-phase induction machine [29]

$T_{e,lim} = 403kNm$	$T_{e,slew} = 12.03MNm/s$
$K = 20$	$\tau = 20ms$
$I_{s,lim} = 1000A$	$v_{dcb} = 5618V$
$K_{pqx} = 17.07V/A$	$K_{pqy} = 17.07V/A$
$K_{iqx} = 306.6V/As$	$K_{iqy} = 306.6V/As$
$K_{pqz} = 61.65V/A$	$K_{iqz} = 504.9V/A$
$\tau_x = 0.2ms$	$\tau_y = 0.2ms$
$\tau_z = 0.2ms$	$\tau_0 = 4ms$
$K_0 = 4.175$	$\lambda^*_{dr} = 44Vs$

Table 6. Parameters of the pulsed power charger [29]

$t_{ch} = 0.8sec$	$t_{ca} = 0.1sec$	$t_{off} = 0.05sec$
$t_d = 0.05sec$	$C_{pp} = 4F$	$L_{pp} = 3.21mH$
$r_{pp} = 2.42\mu H$	$L_c = 64.3\mu H$	$N_{ps} = 5$
$K_{pi} = 0.3213V/A$	$K_{pv} = 80A/V$	$I_{lim} = 6KA$
$V^*_c = 1000V$	$\tau = 4.595ms$	

described in [29] and the parameters are given in table 6. Controlling the charging profile of the storage capacitor requires a firing angle control of the rectifier such that the capacitor voltage follows the desired voltage.

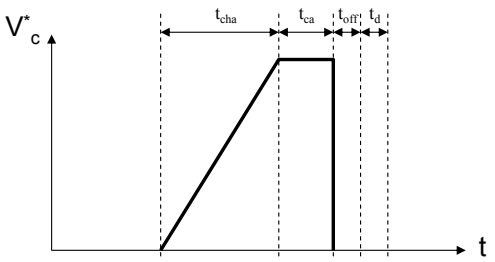

Figure 6. Charging voltage profile for pulsed load.

3. METHODOLOGY

The time-varying random sea spectrum is modeled as a stochastic process, but in addition, we consider that some components of the IM and SM may be described by uncertain parameters. To simulate this coupled stochastic system and analyze its response we use the **probabilistic collocation method** (PCM) and a variance-based sensitivity approach as we describe next.

3.1. Stochastic Modeling – Polynomial Chaos

Polynomial chaos methods are essentially spectral expansions based on Askey-type orthogonal *polynomial functionals* of random vectors. Generalized Polynomial Chaos (gPC) was introduced in [34] as a generalization of the Hermite Chaos expansions originally proposed by Wiener [32].

Let $(\Omega, \mathcal{F}, \mathcal{P})$ be a probability space. A general *second-order* random process, i.e. a process with finite variance, $X(\omega) \in L_2(\Omega, \mathcal{A}, \mathcal{P})$ can be expressed by gPC as

$$X(\omega) = \sum_{i=0}^{\infty} \hat{a}_i \Phi_i(\xi(\omega)), \tag{7}$$

where ω is the random event and $\Phi_i(\xi(\omega))$ are polynomial functionals of degree p in terms of the multi dimensional random variable $\xi = (\xi_1, \ldots, \xi_d)$. The family $\{\Phi_i\}$ is an orthogonal basis in $L_2(\Omega, \mathcal{F}, \mathcal{P})$ with orthogonality relation

$$\langle \Phi_i, \Phi_j \rangle = \langle \Phi_i^2 \rangle \delta_{ij}, \tag{8}$$

where δ_{ij} is the Kronecker delta, and $\langle \cdot, \cdot \rangle$ denote the ensemble average. Here, the ensemble average can be defined as the inner product in the Hilbert space in terms of the random vector ξ

$$\langle f(\xi), g(\xi) \rangle = \int f(\xi) g(\xi) w(\xi) \mathrm{d}\xi \quad \text{or} \tag{9}$$

$$\langle f(\xi), g(\xi) \rangle = \sum_{\xi} f(\xi) g(\xi) w(\xi) \tag{10}$$

in the continuous and discrete case, respectively, where $w(\xi)$ denotes the weight function.

For a certain random vector ξ, the gPC basis $\{\Phi_i\}$ can be selected in such a way that its weight function has the *same* form as the probability distribution function of ξ. The corresponding type of polynomials $\{\Phi_i\}$ and their associated random variable ξ can be found in [34]. For example, *uniform* distributions are represented by Legendre polynomial functionals, *exponential* distributions by Laguerre polynomial functionals, etc. The method includes also *discrete* distributions with corresponding *discrete* eigenfunctions as trial basis; e.g., Poisson distributions are represented by Charlier polynomial functionals.

Equipped with finite-term spectral expansions of the random input and unknown solutions, we can formulate the basic stochastic Galerkin and collocation spectral methods via the usual projections. These procedures essentially recast the stochastic problem as a high-dimensional deterministic problem, whose dimensionality is prescribed by the random input and the order of the approximating polynomials. The stochastic *Galerkin* method usually requires the solution of a system of coupled deterministic problems for the gPC basis coefficients unless the problem is linear in random space. The stochastic *collocation* method [33, 30] (also known as the probabilistic collocation method (PCM)) involves sampling the deterministic system at a set of collocation points chosen to coincide with a numerical cubature rule. Thus, this method is often more easily implemented than gPC in problems with random nonlinearities.

A useful extension to gPC that can handle arbitrary PDFs was the development of the multi-element version [31]. More recently, the multi-element method was formulated for the collocation version of polynomial chaos in [10], thereby extending the sparse-grid integration work of [33]. This last version, which we termed **MEPCM** (*multi-element probabilistic collocation method*), is simply a gPC expansion with collocation (instead of Galerkin) projection on subspaces (elements) of the random space. We have found MEPCM to be superior in terms of *efficiency* over other versions of polynomial chaos for benchmark problems but also for computationally intensive simulations [10, 22].

3.2. Sensitivity Analysis

In the AES, sensitivity analysis can identify the influential and interactive parameters from a large number of parameters needed for the IPS designer to improve performances of the integrated system and to prevent a cascaded failure. Sensitivity analysis, based on the "One-At-a-Time" (OAT) stochastic variation, has been shown to be able to identify and prioritize the important parameters of an AC subsection in the entire IPS [19]. In addition, to further accelerate large-scale simulation and potentially guide experimental studies, a reduction of parametric space can be accomplished by fixing the less important parameters at their nominal values.

The two main classes of techniques for ranking these inputs in sensitivity studies are *local* and *global* methods. The local approach [11, 23], which relies on a partial derivative of output with respect to input, is used to measure the sensitivity around a local operating point. When the system has strong nonlinearity and the input uncertainties are contained within a wide range, the local sensitivity does not provide full information to the IPS designer. On the other hand, the global approach examines the sensitivity from the entire range of the parameter variations. The screening methods, which are included in the global methods, rank the important factors and their interaction among a large number of system parameters. These screening techniques are based on OAT perturbation of parameters, which directly yields the main input effect without input interaction. Several screening methods have been proposed in the literature, for example, the Morris method [16, 25], Cotter's method [7], factorial experimentation [2], and iterated fractional factorial design [24]. The different approaches have their strengths and weaknesses. The Morris method can efficiently identify the sensitive parameters when a system has a large number of inputs or parameters. Only the worst-case analysis of a system is examined for the upper and lower bounds of system variables in Cotter's method. In factorial experimentation, all combinations of inputs' interactions as well as the main effects are evaluated at the same time, which requires intensive computation. Iterated fractional factor design reduces this large input-combination computation by evaluating only important combinations but the sensitivity indices might be biased.

To investigate the OAT global sensitivity, an elementary effect of i input on j output (EE_i^j) is defined as the approximated gradient. Basically, EE_i^j is a ratio of the difference in outputs $y_j(\mathbf{x})$ over Δ when only i input deviates from its nominal value with Δ magnitude. This definition of EE_i^j is identical to that of Morris [16]. The EE_i^j can be formulated as:

$$EE_i^j = \frac{y_j(x_1, x_2, \ldots, x_i + \Delta, \ldots, x_k) - y_j(x_1, x_2, \ldots, x_i, \ldots, x_k)}{\Delta},$$

where x_i with $i = 1, \ldots, k$ is contained within a domain of variation. For y_j outputs with $j = 1, \ldots, n$, we need a total of $n \times k$ computations of EE_i^j. Using the local gradient computation, when $\partial y_j / \partial x_i$ is equal to 1) zero, 2) a non-zero constant, or 3) a non-constant function of input parameter/s, the effects of x_i on y_j are 1) negligible,

2) linear and additive, or 3) nonlinear and coupled, respectively. The numerically approximated gradient can capture all the above effects – it is called the *elementary* or first-order effect. If all x except x_i are fixed at their nominal values, the EE_i^j can only rank the input parameter according to the first-order or elementary effect without specifying any influence of the interaction among inputs. However, by randomizing all values of $\mathbf{x}$ in computing EE_i^j, the interaction effects can be discovered from the variation of the EE_i^j distribution.

In [22], four sensitivity analysis techniques for ranking the inputs' significance and the nonlinear and coupling effects of inputs were studied. Two of them were based on *gradient-based* analysis while the other two were based on *variance-based analysis*. Gradient-based methods, while effective in general, can be very costly and are not so accurate for non-smooth solutions. The regularity required for computing the local gradient at one point in a parameter range to be representative of the gradient over the entire range is not guaranteed nor expected for a nonlinear system like IPS. To this end, we also consider variance-based methods and investigate their connection to gradient-based methods. Specifically, we make some mathematical connections between MEPCM local variance-based sensitivity techniques and gradient-based methods. Let us focus on a particular hypercube element B, a subset of the N-dimensional parametric space, written without loss of generality as the product set $\prod_{i=1}^{N}[x_{0,i}-h, x_{0,i}+h]$ where $x_0 = (x_{0,1}, x_{0,2}, ..., x_{0,N})$ is the center of B. Suppose we have a function $f \in C^3(B)$ and assume X is a random variable uniformly distributed on B. It can be shown [9] that the variance of $f(X)$ over B^i, when normalized with the one-dimensional uniform distribution variance, approximates the norm of the gradient $\|\nabla f|_{x_0}\|^2$ in the limit as $h \to 0^+$. This result is easily generalizable to rectangular B, but we will assume uniform edge lengths for simplicity here. Specifically, we have:

$$\frac{\mathrm{Var}_B[f(X)]}{\frac{h^2}{3}} = \|\nabla f|_{x_0}\|^2 + O(h^2).$$

The rate of convergence here is $O(h^2)$, which is independent of N. Hence, we see that the variance-based sensitivity analysis is related to the gradient-based sensitivity analysis as indicated in the above relationship.

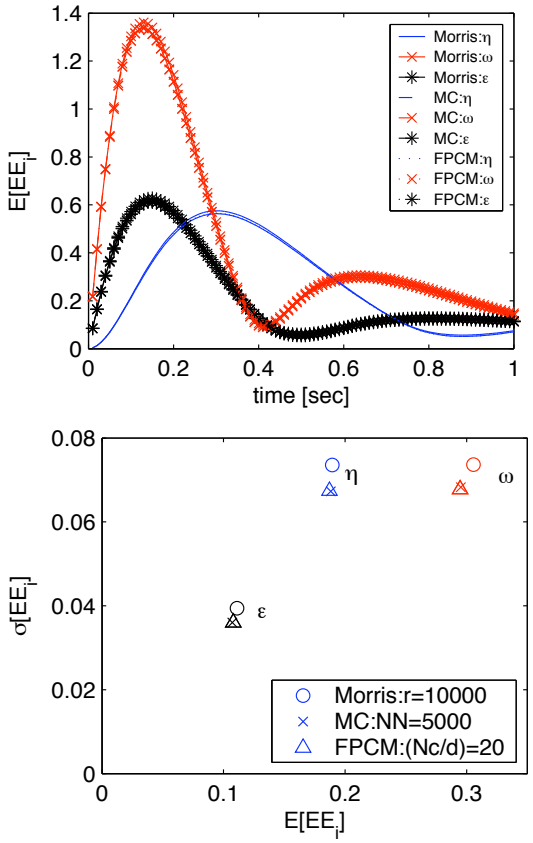

Figure 7. Duffing's oscillator: Top - Mean sensitivity $E[EE_i]$ of η, ω, and ε as a function of time, $t \in [0,1]$ seconds, using the Morris method (solid-line), the Monte Carlo Sampling (MC) (dash-line), and Collocation method (FPCM) (dot-line). Bottom: Interaction effect $\sigma[EE_i]$ versus mean sensitivity $E[EE_i]$ at fixed time $t = 2/3$ seconds.

3.3. Example: Stochastic Duffing's Oscillator

Having discussed the use of polynomial chaos and in particular MEPCM in solving stochastic differential equations we present an example, namely the nonlinear Duffing oscillator, to demonstrate the results of sensitivity analysis. The governing equation is

$$\frac{dy^2}{dt} + 2\eta\omega\frac{dy}{dt} + \omega^2 y + \varepsilon\omega^2 y^3 = 1.0, \qquad (11)$$

with $dy(0)/dt = 0; y(0) = 2$, where η, ω, and ε are the damping coefficient, natural frequency, and coefficient of the cubic nonlinearity. All η, ω, and ε are assumed to be independent *uniform random variables* with mean of 2 and standard deviation of 0.2 for unbiased weighting. From this nonlinear system, ω is the most influential

parameter due to the quadratic nonlinearity and strong coupling with the other two terms of the equation. However, this might not be the case for all times between [0,1] seconds. We will use the mean value of the elementary effect, $E[EE_i]$, to quantify the sensitivity and the standard deviation, $\sigma[EE_i]$, to quantify the interaction between parameters. As shown in Figure 7(top), the trajectories of normalized $E[EE_i]$ for the three random parameters are plotted as a function of time using the Morris method, the Monte Carlo Sampling and Collocation methods with $\Delta = \frac{1}{2}$, which are based on the gradient computation; similar results are obtained also with the variance-based methods [22]. Note that the normalized $E[EE_i]$ trajectories from the Monte Carlo and Collocation methods are identical and also match closely that of the Morris method. From the plot of normalized $E[EE_i]$ versus time, the sensitivity effect of ω is dominant at the first quarter of a second and again after 0.6 seconds; the damping effect of η surpasses that of ω only between 0.35 and 0.6 seconds. These changing trends occur because of the cubic nonlinearity in the last term of the Duffing equation. In addition, we can consider the ranking of inputs' first-order and coupling effects at a specified time, as shown in Figure 7(bottom) for t=$\frac{2}{3}$ seconds. For the values chosen, the interaction effects of η and ω are about the same at this fixed time instant whereas at earlier times the interaction effect of ω dominates.

4. IPS RESULTS

We now return to the IPS and consider the coupled IPS-Hydrodynamics stochastic system; here we simulated the surge motion of the electric ship excited by the Pierson and Moskowitz spectrum with $H^{1/3} = 20$ ft. The interaction between the ship speed, propulsion load, and electric machines' states are examined for sea state 6, very rough sea [3]. Two identical IPS, as shown in Figure 1, with the torque control using the IFOC, directly connected to the propeller, drive the 1DOF ship motion in head and random seas, see Figure 2. We note that this is a simplified model and does not correspond to the full DDG-51 configuration which requires 4 IPS to reach 31 knots, see table 1. Here we further assume that initially two generators operate near their steady-state conditions and then after 2 seconds the two propulsion drives are turned on while the ship moves forward at about *20 knots*. The mean added resistance and the slowly-varying added resistance of the scaled electric ship are computed using Newman's approximation and the added resistance response amplitude operator [18]. Thus, the propellers driven by IPS experienced the slow-varying force from the added resistance.

In this section, we simulate the effects of both the *propeller emergence* and the *pulsed power load charger* on the IPS. First, we consider only the induction motor drive with a *constant* voltage supply in order to tune the field-oriented controller. Second, we consider the entire IPS that includes the generator, bus and the IM drive connected to a propeller. These machines exhibit a *strong interaction* when they are first connected together due to start up dynamics and have to be turned on sequentially. In this case, we investigate the ship surge motion driven by the highly skewed propeller connected to the IPS. Finally, a 5 MW pulsed power charge is added to the IPS's AC distribution system in order to examine the effect of a sudden large load propagating through the entire IPS. We also present stochastic simulations that take into account the uncertainty associated with two parameters of IPS.

4.1. Parameter Sensitivity

First, in order to check that the field-oriented control of the 15-phase induction machine (IM) is working properly, we separate the 19 MW IM drive from the generator and distribution bus in order to tune separately the parameters of IM drive. The controller of IM is independently provided with a constant 3-phase voltage (V_{abc}), supplying the 3 parallel rectifier dc link paths, as shown in Figure 8. In this model, a *simplified* hydrodynamics model from [29] is used as a torque load.

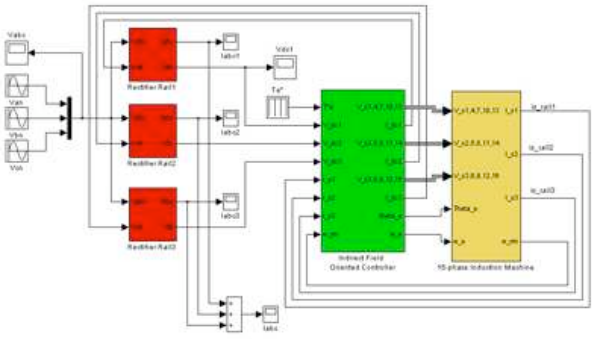

Figure 8. Simulink diagram of the field-orient control of 15-phase induction machine.

Initially, the induction machine is started from rest with a small constant torque command of 1000 N-m and then at 10 seconds the torque command is increased to 8×10^5 N-m. Using the controller parameters (slew rate ($T_{slew} = 4 \times 10^6$) and proportional gain ($K = 100$) reported in [29] leads to large overshoots in both machine torque and rectifier dc current, as shown in Figures 9 and 10. The gain K of the torque limiter for each rail must be decreased to reduce overshoots in IM drive's response, but the slew rate (T_{slew}) of torque limiter need to be increased to reduce response time of the IM torque T_e and Rectifier dc current I_{dc}. Thus, we will use the values of $K = 20$ and $T_{slew} = 12 \times 10^6$ in the rest of the paper. Note that the proportional and integral gains of the XYZ current control have only minor effect on the large overshoot corresponding to the step torque command.

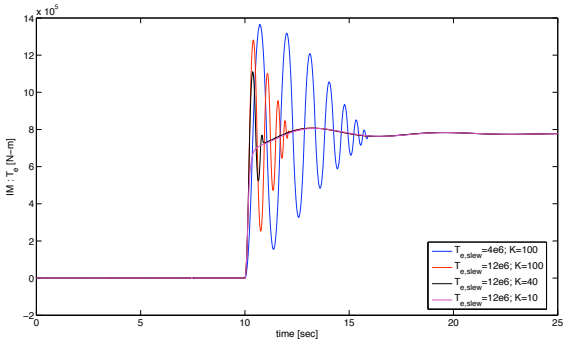

Figure 9. Step change: Induction machine torque with different K and T_{slew}.

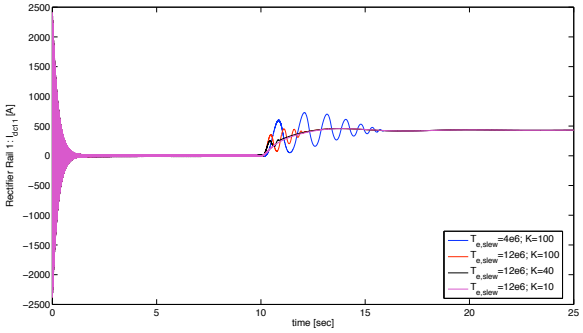

Figure 10. Step change: The first 5-phase rectifier dc current with different K and T_{slew}.

Next, we examine the specific effects of propeller emergence that causes a load torque reduction on the IM drive. Given a constant voltage source, the 15-phase motor drive connected to a Boswell's highly skewed propeller [1], we allow only surge motion of the ship in a head sea corresponding to Pierson and Moskowitz spectrum with $H^{1/3}$ = 20 ft. The effective disc area of the propeller is reduced when the propeller emerges out of water. We note that the thrust loss factor, β_T, and the torque loss factor, β_Q, should be multipleed by the propeller thrust and torque, respectively. The propeller emergence leads to an increase in motor's or propeller's angular speed by about 7% and a negligible change in ship speed, as shown in Figure 11. Furthermore, in Figure 12, the phase current of induction first decreases and subsequently increases while the propeller is out of the water. However, the rectifier phase current must be increased slightly to compensate for an abrupt increase in IM's speed.

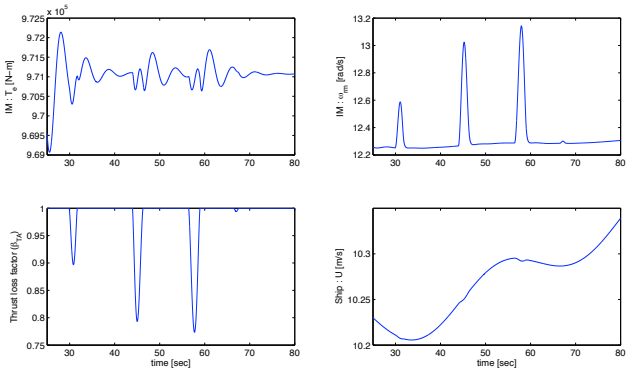

Figure 11. Propeller emergence: Responses of the IM's torque, IM's angular speed, and ship speed due to the thrust and torque reduction.

4.2. Pulsed Power Load

To examine the effect of a 5 MW pulsed power load on the entire system, in this scenario, the generator and bus are operated near their steady state condition and then at time = 0.5 seconds, the IM drive, also operating close to its steady state, is turned on with a constant torque command of 9.25×10^5 N-m. The pulsed power charger is switched on at 6 seconds and, in addition, the thrust loss factor is imposed at the propeller thrust and torque at the same time. There are sudden increases and decreases in the SM current and bus voltage because a relatively large power is instantaneously drawn from the bus to support the pulsed power charger. Consequently,

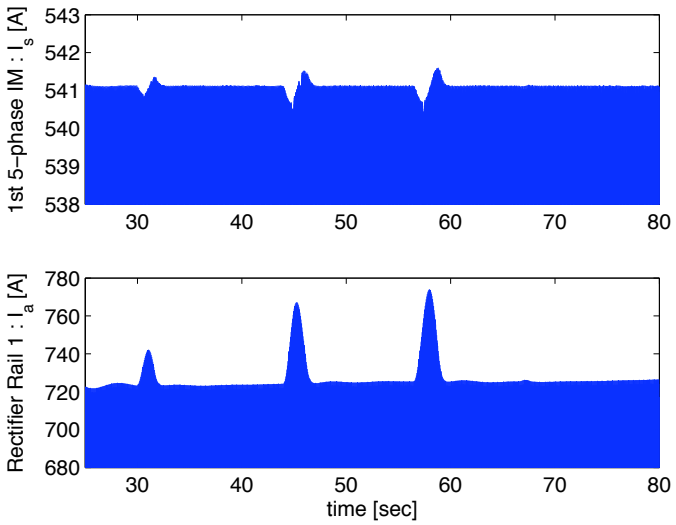

Figure 12. Propeller emergence: Responses of the IM's and rectifier's phase currents due to the thrust and torque reduction.

the SM torque increases and the exciter tries to increase the field-winding voltage to maintain the voltage at a constant level. However, only minor effects are exhibited in the IM torque and angular speed due to the pulsed power charge, as shown in Figure 13 14, 14, 15, and 16 (with an enlargement scale). The IM speed again increases with the torque loss as a result of the propeller emergence.

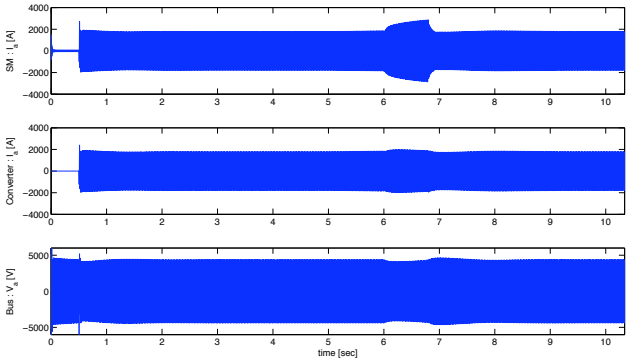

Figure 13. Responses of generator and induction motor phase-current and bus phase-voltage due to charging a pulsed power charger at time = 6 seconds.

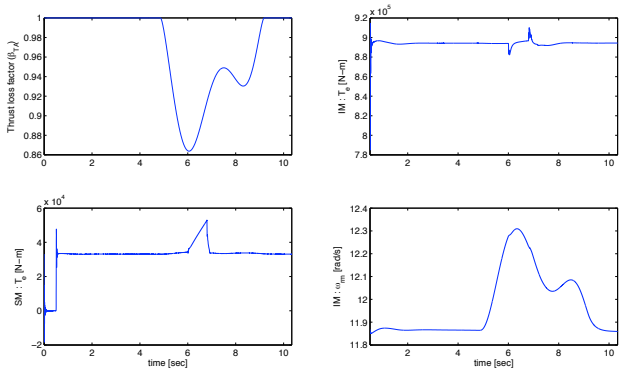

Figure 14. Responses of generator and induction motor torque and angular speed due to charging a pulsed power charger at time = 6 seconds.

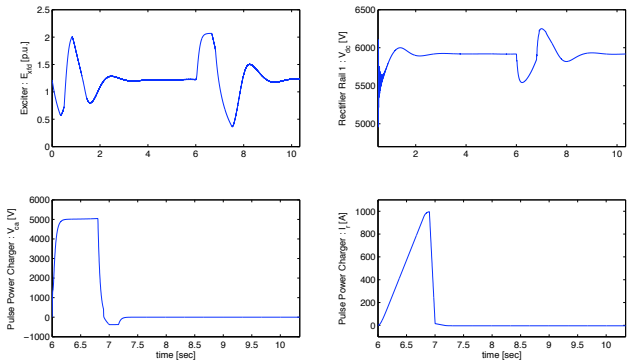

Figure 15. Responses of exciter field-winding voltage, rectifier rail 1 voltage, capacitor voltage (V_{ca}) of pulse power charger, and inductor current (I_r) of pulsed power charger due to charging a pulsed power charger at time = 6 seconds.

4.3. Stochastic Simulations

We now consider both the SM field-winding resistance, r_{fd}, and the IM rotor inertia, J, to be *uniform random variables* with 20% variation from their nominal values. Our objective is to examine the stochastic responses of SM, exciter, IM, Ship, and pulsed power charger because of the uncertainty propagation from these parameters. Using a full-grid collocation method (FPCM) [22], stochastic variations of all system responses can be computed from the 25-point Gauss-Legendre quadrature. Specifically, the sampling points are simply fixed points in the parameter space defined by the roots of the Legendre orthogonal polynomials employed in the representation of all stochastic fields.

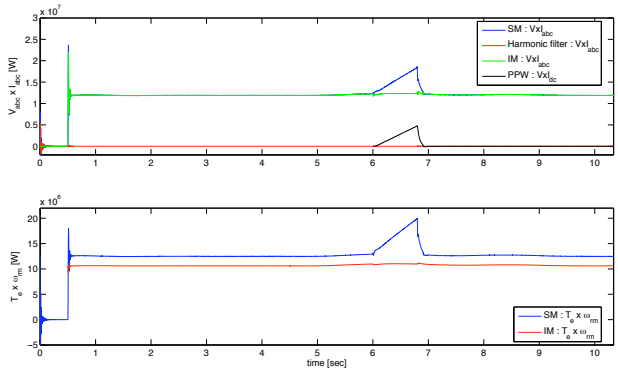

Figure 16. Responses of instantaneous electrical and mechanical power from both generator, bus, induction motor, harmonic filter, and pulsed power charger due to charging a pulsed power charger at time = 6 seconds.

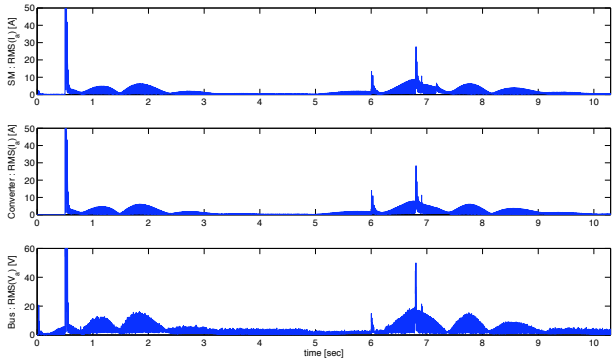

Figure 17. Root-mean square responses of generator and induction motor phase-current and bus phase-voltage due to charging a pulsed power charger at time = 6 seconds.

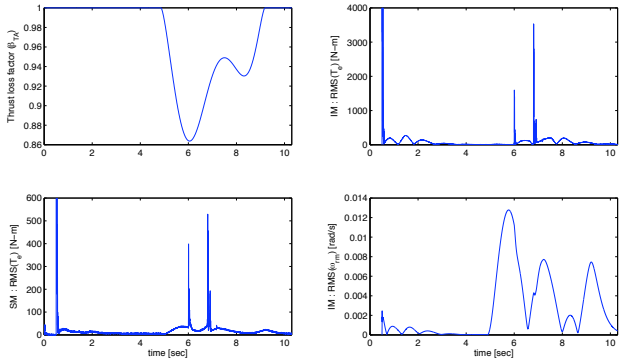

Figure 18. Root-mean square responses of generator and induction motor torque (T_e) and angular speed (ω_{rm}) due to charging a pulsed power charger at time = 6 seconds.

A variation in r_{fd} might be caused by an operational temperature dependence. On the other hand, the value of IM rotor inertia is not readily available in the literature and hence it can be modeled as uncertain parameter. The same scenario as in the previous case is considered. Figure 17, plotting the root-mean square or standard deviation, shows strong variation in SM and IM phase-currents and bus phase voltage only when IM is turned on near its steady state condition. Then, root-mean square values of these currents and voltage oscillate with small magnitude. There are large variations in SM and IM torque, but variations in both IM angular speed and ship forward speed are small, as seen in Figure 18 and 19. However, Figure 20 shows a non-negligible effect on the exciter field-winding voltage and rectifier dc voltage due to these uncertainties. This indicates the importance of knowing the precise value of r_{fd}, which we have also verified with more elementary parametric studies.

5. CONCLUSION

We have presented detailed models for the two primary components of the All-Electric Ship (AES), namely the Integrated Power System (IPS) and the Hydrodynamics. This is the first time that all components of each system have been modeled and coupled together at this level. Simulating such a coupled system on today's computers is feasible, and results can be obtained in a matter of minutes – even for long-time integration of the system – to include the characteristic electric, mechanical and hydrodynamic scales. We note that these characteristic time scales, even of the small subcomponents, are not input to the problem but they are part of the solution, unlike other models where simplified lumped parametrizations are employed. In addition we have demonstrated how we can use polynomial chaos representations to model parametric uncertainties in some of the compoents of the electromechanical system. This, in turn, allows us to expeditiously quantify the global sensitivity of the system – a very important component in design process. For example, in the case we simulated stochastically we showed that the SM field winding resistance, r_{fd}, has a big effect on the exciter that controls the voltage of the SM. Our aim in this

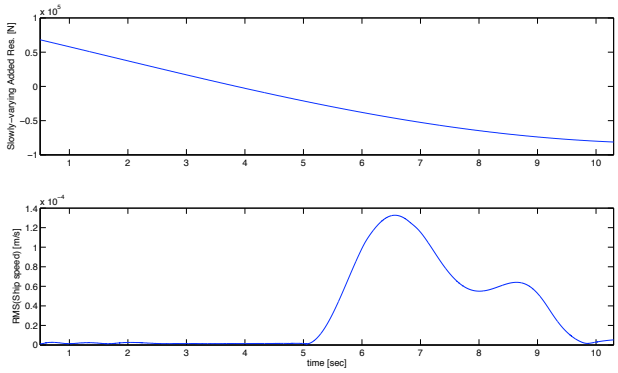

Figure 19. Root-mean square responses of Ship Speed and magnitude of slowly varying added resistance.

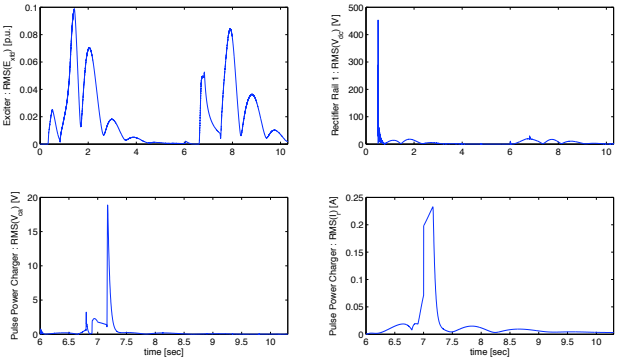

Figure 20. Root-mean square responses of exciter field-winding voltage, rectifier rail 1 voltage, capacitor voltage (V_{ca}) of pulse power charger, and inductor current (I_r) of pulse power charger due to charging a pulsed power charger at time = 6 seconds.

first paper was to demonstrate the capability of the new framework, and we will report more systematic sensitivity studies in future work.

ACKNOWLEDGMENT

This work is supported by the Office of Naval Research (N00014-02-1-0623 ESRD Consortium, Also N00014-07-1-0846) and Sea Grant (NA060AR4170019 NOAA/DOC).

REFERENCES

[1] Boswell R.J., Design, Cavitation Performance, And Open-Water Performance Of A Series of Research Skewed Propellers, *Report 3339, Department Of The NAVY, Naval Ship Research And Development Center*, March 1971.

[2] Box, G.E.P., Hunter W.G., and Hunter J.S., *Statistics for Experimenters. An Introduction to Design, Data Analysis and Model Building*, Wiley, New York, 1978.

[3] Carlton J.S., *Marine Propellers and Propulsion*, first edition, Butterworth-Heinemann Ltd, 1994.

[4] Chaboki A., Thurmond L., Grater G., Bauer D., Beach F., and Clayton D., Integration of electromagnetic rail gun into future electric warship, *High Powered Weapons Systems for Electric Ship Conference*, Dec. 2004.

[5] Chryssostomidis C. and Steen A, MIT5D Seakeeping Computer program, MIT, Department of Ocean Engineering, 1974.

[6] Clayton D.H., Sudhoff S.D., Grater G.F. ,Electric Ship Drive and Power System, *Conf. Rec. 2000 24th Int. Power Modulation Symp.*, 2000, pp. 85-88.

[7] Cotter, S.C., A screening design for factorial experiments with interactions, *Biometrika*, Vol. 66, pp. 317-320, 1979.

[8] Dalzell J.F., Kim C.H., An Analysis of the Quadratic Frequency Response for Added Resistance, *Journal of Ship Research*, Vol. 23, No. 3, pp. 198-208, 1979.

[9] Foo J., Multi-element probabilistic collocation in high dimensions: Applications to systems biology and physical systems, Division of Applied Mathematics, Brown University, 2008.

[10] Foo ,J., X. Wan and G.E. Karniadakis, 'The multi-element probabilistic collocaiton method (ME-PCM): Error analysis and applications, *J.Comp. Phys.*, vol. 227(22), pp. 9572-9595, 2008.

[11] Hockenberry, J.R., Evaluation of Uncertainty in Dynamic, Reduced-Order Power System Models, Ph.D. thesis, Massachusetts Institute of Technology, 2000.

[12] IEEE Committee Report, Computer Representation of Excitation Systems, *IEEE Trans. on Power Apparatus and Systems*, Vol. PAS-87, pp. 1460-1464, June 1968.

[13] Lewis E.V. (Editor), *Principles of Naval Architecture*, Second Revision, The Society of Naval Architects and Marine Engineers, NJ, 1989.

[14] Krause P.C., Wasynczuk O., and Sudhoff S.D., *Analysis of Electric Machinery and Drive Systems*, Second Edition, IEEE Press and Wiley-Interscience, NY, 2002.

[15] Military Analysis Network, Federation of American Scientists, DDG-51 Arleigh Burke-class, "http://www.fas.org/man/dod-101/sys/ship/ddg-51.htm".

[16] Morris, M.D., Factorial Sampling Plans for Preliminary Computational Experiments, *Technometrics*, Vol. 33, No. 2, pp. 161-174, May 1991.

[17] Newman J.N., *Marine Hydrodynamics*, Ninth Edition, The MIT Press, MA, 1999.

[18] Newman J.N., Second-order, Slowly-Varying Forces on Vessels in Irregular Waves, *Paper 19, International Symposium on Dynamics of Marine Vehicles and Structures in Waves*, London, April 1999.

[19] PC Krause and Associates, Power System Control Development, Final Report, Contract F33615-99-D-2974 for NSF/ONR Partnership in Electric Power Network Efficiency and Security (EPNES), March 2003.

[20] Salvesen N., Second-order Steady-State Forces and Moments on Surface Ships in Oblique Regular Waves, *Paper 22, International Symposium on Dynamics of Marine Vehicles and Structures in Waves*, London, April 1999.

[21] Smogeli Ø.V., Control of Marine Propellers From Normal to Extreme Conditions, Ph.D. thesis, Norwegian University of Science and Technology, 2006.

[22] Prempraneerach P., Uncertainty Analysis in a Shipboard Integrated Power System using Multi-Element Polynomial Chaos, Ph.D. thesis, Massachusetts Institute of Technology, 2007.

[23] Rabitz, H., Kramer M., and Dacol D., Sensitivitiy analysis in chemical kinetics, *Annu. Rev. Phys. Chem.*, Vol. 34, pp. 419-461, 1983.

[24] Saltelli A., Andres T.H., Homma T., Sensitivity analysis of model output. Performance of the iterated fractional factorial design method, *Computational statistics and data analysis*, Vol. 20, No. 4, pp.387-407, 1995

[25] Saltelli A., Chan K., Scott M., *Sensitivity Analysis*, John Wiley & Sons Ltd, 2000.

[26] Sudhoff S.D., Corzine K.A., Glover S., Hegner H.N. Robey, Jr., DC Link Stabilized Field Oriented Control of Electric Propulsion Systems, *IEEE Trans. on Energy Conversion*, Vol. 13, No. 1, March 1998.

[27] Sudhoff S.D., Kuhn B.T., Zivi E., Delisle D.E., and Clayton D., Impact of Pulsed Power Loads on Naval Power and Propulsion Systems, *Electric Ship Research and Development Consortium (ESRDC)*, Recent Papers, nerc.aticorp.org/esrdc_recent_papers.html.

[28] Sudhoff S.D., Pekarek S., Kuhn B., Glover S., Sauer J., Delisle D., Naval Combat Survivability Testbeds for Investigation of Issues in Shipboard Power Electronics Based Power and Propulsion Systems, *Power Engineering Society Summer Meeting, IEEE*, Vol. 1, pp. 347 - 350, July 2002.

[29] Sudhoff S.D., Wasynczuk O., Krause P.C., Dynamic Simulation of High-Power Machinery, *Final Report to Naval Surface Warfare Center*, Carderock Division, Annapolis Detachment, Contract N61533-95-C-0107, July 1996.

[30] Tatang, M. and G. McRae, "Direct Treatment of Uncertainty in Models of Reaction and Transport", *MIT Technical Reports*, 1994.

[31] Wan, X. and G. E. Karniadakis, Multi-element generalized polynomial chaos for arbitrary probability measures, *SIAM J. Sci. Comput.*, vol. 28, pp. 901-928, 2006.

[32] Wiener, N., "The homogeneous chaos", *American Journal of Mathematics*, vol. 60, pp. 897-936, 1938.

[33] Xiu, D. and J. Hesthaven, "High-Order Collocation Methods for Differential Equations with Random Inputs", *SIAM J. Sci. Comput.*, vol. 27, pp. 1118–1139, 2005.

[34] Xiu, D. and G. E. Karniadakis, The Wiener-Askey polynomial chaos for stochastic differential equations, *SIAM J. Sci. Comput.*, vol. 24, pp. 619–644, 2002.

[35] Zivi E., McCoy T.J., Control of a Shipboard Integrated Power System, *Proceedings of the 33th Annual Conference on Information Sciences and Systems*, March 1999.

P. Prempraneerach *received his PhD from MIT in 2007 and he is currently Lecturer and Researcher at the Department of Mechanical Engineering at Rajamangala University of Technology in Thailand. He is also a Visiting Research Scientist at the MIT Sea Grant. His interests are in power systems and power electronics, robotics, seakeeping and uncertainty analysis.*

J. Kirtley *is Professor of Electrical Engineering at MIT and Director of Satcon Technology Corporation. He has made significant contributions to the design, analysis, and construction of high performance electric machinery. His work spans from energy conversion to high-speed transportation. He served as editor-in-chief of the IEEE Transactions on Energy Conversion from 1998 to 2006 and he is a member of the National Academy of Engineering.*

C. Chryssostomidis *is Director of the MIT Sea Grant College Program and Doherty Professor of Ocean Science and Engineering at MIT. He is the founder of the MIT Autonomous Underwater Vehicles Laboratory (AUV) and has led many AUV expeditions in the Mediterranean. His interests include ship design, vortex-induced vibrations, and underwater vehicle design.*

M.S. Triantafyllou *is the William I. Koch Professor of Marine Technology, Associate Department Head, and Director of the Center for Ocean Engineering in the Mechanical Engineering Department at MIT. His research interests are biomimetics, vortex dynamics, flow-structure interactions and control.*

G.E. Karniadakis *is Professor of Applied Mathematics at Brown University and Senior Lecturer of Mechanical Engineering at MIT. His interests are large-scale simulations, multiscale modeling and uncertainty quantification for physical and biological systems. He has published three books and over 250 research papers.*